Research in Astron. Astrophys. **2011** Vol. **11** No. **8**, 909–923
http://www.raa-journal.org *http://www.iop.org/journals/raa*

***R**esearch in*
***A**stronomy and*
***A**strophysics*

Stellar kinematics and populations out to 1.5 effective radii in the elliptical galaxy NGC 4636 *

Shi-Bi Pu[1,2,3] and Zhan-Wen Han[1,3]

[1] National Astronomical Observatory / Yunnan Observatory, Chinese Academy of Sciences, Kunming 650011, China; *pushibi@hotmail.com*
[2] Graduate University of Chinese Academy of Sciences, Beijing 100049, China
[3] Key Laboratory of the Structure and Evolution of Celestial Objects, Chinese Academy of Sciences, Kunming 650011, China

Received 2011 March 9; accepted 2011 April 20

Abstract We present high quality long slit spectra along the major and minor axes out to 1.5 effective radii of the massive galaxy NGC 4636 taken by the Hobby-Eberly Telescope. Using the Fourier Correlation Quotient method, we measured the stellar line-of-sight velocity distribution along the axes. Furthermore, six Lick/IDS indices (Hβ, Mgb, Fe$_{5015}$, Fe$_{5270}$, Fe$_{5335}$, Fe$_{5406}$) are derived from the clean spectrum. By comparing the measured absorption line strengths with the predictions of Simple Stellar Population (SSP) models, we derived ages, total metallicity and α abundance profiles of the galaxy. This galaxy presents old and [α/Fe] overabundant stellar populations. Indeed, using the SSP model, we obtained the broadband color profiles. The theoretical colors match well with the measured colors and present red sharp peaks at the galaxy center. The sharp peaks of the colors are mainly shaped by the high metallicity in the galaxy's center. Interestingly, the galaxy has steep negative metallicity gradients, but the trend flattens outwards. This result likely suggests that the center and outer regions of the galaxy formed through different formation processes.

Key words: galaxy: elliptical and lenticular — galaxy: abundances — galaxy: kinematic and dynamics — galaxy: individual (NGC 4636)

1 INTRODUCTION

The formation and evolution of massive, early-type galaxies constitutes a long-standing and crucial problem in cosmology (Sánchez-Blázquez et al. 2007). According to the classic *monolithic-collapse* model for the formation and evolution of early-type galaxies (Tinsley 1972; Larson 1975; Tantalo et al. 1996), early-type galaxies formed most of their stars during a single short and highly efficient star formation event in the early universe. This model is strongly supported by the extremely small scatter of the observed color magnitude relation of elliptical galaxies. This uniformity of stellar populations in ellipticals is also supported by the Fundamental Plane (Dressler et al. 1987; Djorgovski & Davis 1987; Bender et al. 1992; Saglia et al. 1993). Moreover, the tightness of the Mg-σ relation for massive elliptical galaxies observed in the local universe (Bender et al. 1993; Sánchez-Blázquez

* Supported by the National Natural Science Foundation of China.

et al. 2007) near the intermediate redshift $z \approx 1$ (Ziegler & Bender 1997; Bender et al. 1998) requires a picture of a short and highly efficient star formation process at high redshift and passive evolution subsequently.

In contrast, according to the *hierarchical merging* scenario (White & Rees 1978; Kauffmann et al. 1993), massive early-type galaxies are expected to have formed through multiple mergers and accretion of smaller objects over an extended period (White & Frenk 1991; Somerville & Primack 1999; De Lucia et al. 2006). This formation scenario has been observationally confirmed; COMBO-17 and DEEP2 surveys show that the number density of red galaxies has increased since redshift $z = 1$ (Bell et al. 2004; Faber et al. 2007). Furthermore, giant galaxies show boxy isophotes and anisotropic dynamics and more massive galaxies are more radio-loud, stronger X-ray emitters, and are more frequently active. By contrast, normal and low luminosity elliptical galaxies rotate rapidly, are nearly isotropic, and show disky distorted isophotes and cuspy inner profiles. The properties of the former can be explained in dissipationless mergers, while the latter are recovered successfully with dissipational mergers (Nieto & Bender 1989; Bender et al. 1989; Bender & Surma 1992; Barnes 1992; Mehlert et al. 1998). Recently, Kuntschner (2000); Thomas et al. (2005); Collobert et al. (2006); Bernardi et al. (2006); Clemens et al. (2006); Rogers et al. (2010) showed that early-type galaxies in low density and in high density environments might exhibit different formation ages and Lisker & Han (2008); Sánchez-Blázquez et al. (2009); Matković et al. (2009) found evidence that lower mass galaxies have more extended star formation histories.

Radial profiles of the kinematics, colors, ages and metallicities of the stellar populations are efficient tools to study galaxy formation scenarios. In standard closed-box models of chemical enrichment, the metallicity is a function of the yield and of how much gas has been locked after star formation has ceased (Tinsley 1980). Therefore, the metallicity strongly depends on the associated dynamical parameters. For instance, for galaxies formed via a *monolithic-collapse*, stars formed in all regions during the collapse and remain in their orbits with little movement inward, whereas the gas dissipates into the center, being continuously enriched by the evolving stars. Therefore, stars formed in the center are predicted to be more metal rich than those in the outer regions. These galaxies should have steep radial metallicity gradients (Larson 1976; Thomas 1999; Sánchez-Blázquez et al. 2007). On the other hand, major mergers, which follow the *hierarchical merging* scenario, will dilute stellar population gradients (White 1980; Kobayashi 2004; Hopkins et al. 2009; Tortora et al. 2011). Therefore, more flat population gradients are expected within this picture. Accordingly, the observation of stellar population gradients and their connection to dynamical parameters can give crucial insight into the formation paths of individual galaxies.

This work aims to deeply investigate the stellar kinematics and populations of the massive galaxy NGC 4636. NGC 4636 is an E/S0 galaxy, located about 2.8 Mpc southeast from the Virgo center and 14.7 Mpc [$(m - M)_0$ = 30.83 ± 0.13] from us. Effective radius, ellipticity and position angle of the major axis of NGC 4636 are $R_\mathrm{e} = 88.5''$, ϵ_e =0.256 and PA= 150°, respectively (Tonry et al. 2001; Rampazzo et al. 2005; Kim et al. 2006; Schuberth et al. 2006). NGC 4636 is considered to be a major member of a small group falling into the Virgo center (Nolthenius 1993). Although it is relatively less luminous (M_v = –21.7 mag) among the gEs in Virgo, NGC 4636 shows several interesting features. For instance, NGC 4636 is found to be very bright in X-rays ($L_\mathrm{X} \sim 10^{41}$ erg s^{-1}), with an unusual feature in the hot interstellar medium (ISM) (O'Sullivan et al. 2005; Kim et al. 2006; Posson-Brown et al. 2009). The galaxy NGC 4636 has boxy isophotes (Rembold et al. 2002) and does not show rotation along either its major or minor axes (Davies et al. 1993; Bender et al. 1994; Rampazzo et al. 2005). Indeed, NGC 4636 is one of the best targets for studying kinematics of globular clusters (GCs) since it has an anomalously large number of GCs (Dirsch et al. 2005; Chakrabarty & Raychaudhury 2008; Park et al. 2010; Lee et al. 2010).

There are a number of works which focus on the study of kinematic profiles, line strength indices and stellar population parameters in NGC 4636 (Davies et al. 1993; Bender et al. 1994; Tantalo et al. 1998; Rampazzo et al. 2005; Annibali et al. 2006; Li et al. 2007). However, the previous measurements were concentrated within R_e/2 of the galaxies. From a comparison of the stellar parameters within R_e/8 with those within R_e/2 of some early-type galaxies sample, Davies et al. (1993); Trager et al. (2000); Denicoló et al. (2005) found that the elliptical galaxies present slightly negative metallicity gradients from their centers to the outer regions and the ages are likely to increase slightly outwards. The same trends were detected by Fisher et al. (1995). However, only 1/3 of the star mass is contained within R_e/2. In this work, we obtained deep long slit spectra of the local galaxy NGC 4636 outwards to 1.5 R_e, aiming to study the stellar populations and kinematics out to larger radii and find crucial insight into the formation paths of a galaxy.

The paper is organized as follows. In Section 2 we describe the observations (Sect. 2.1) and the data reduction (Sect. 2.2). In Section 3 we present the kinematics (Sect. 3.1) and the line strength measurements (Sect. 3.2). We analyze the Lick indices and derive ages, metallicities and α/Fe ratios, present the colors and mass-to-light ratios and briefly describe the models and the method used in Section 4. A summary of this work is presented in Section 5. The full data tables of kinematics and Lick/IDS indices are shown in Appendix.

2 OBSERVATIONS AND DATA REDUCTION

2.1 Observation

Long-slit spectra along major and minor axes of NGC 4636 were collected during the period of April to May in 2008 using the HET in service mode and the Low-Resolution Spectrograph (LRS) with the E2 grism (Hill et al. 1998). In order to detect the galaxy's outer regions, the center of the galaxy was moved towards one end of the slit. The slit width was 3″, giving an instrumental broadening of $\sigma_{\rm inst}$ = 120 $\rm km\ s^{-1}$ and covering the wavelength range from 4790 Å to 5850 Å. The exposure time of each slit was 900 s. Moreover, 900 s exposures of blank sky regions were taken at regular intervals. The seeing ranged from 1.49″ to 2.57″. The resulting summed spectrally-probed regions extend out to nearly 1.5 R_e of NGC 4636. In addition, calibration frames (biases, dome flats and the Ne and Cd lamps) were taken. Table 1 shows the logs of the spectroscopic observations.

Table 1 Log of Spectroscopic Observation (MJ = major axis, MN = minor axis, SKY= sky spectrum)

Date	Objects	Position	Seeing (FWHM)
2008 Apr 04	NGC 4636	MJ1, SKY1	2.57
2008 Apr 06		MJ2, 3, SKY2	1.49
2008 Apr 09		MJ4, 5, SKY3	1.64
2008 May 01		MN1, 2, SKY4	1.92

Notes: The exposure time for each slit is 900 s. Position angles of major and minor axes of NGC 4636 are 150° and 60° respectively.

2.2 Data Reduction

The data reduction used the MIDAS package provided by ESO. The pre-processing of the data reduction was done following Bender et al. (1994). The raw spectra were bias subtracted and divided by the flat fields. The cosmic rays were removed with a $\kappa - \sigma$ clipping procedure. The wavelength calibration was performed using 9 to 11 strong Ne and Cd emission lines and a third order polynomial. The achieved accuracy of the wavelength calibration was always better than 0.6 Å (rms). The science spectra were rebinned to a logarithmic wavelength scale.

The step of sky subtraction required particular care to minimize systematic effects on the measured kinematics and line strengths in the outer regions of our galaxies. More details can be seen in Saglia et al. (2010, fig. 2) and Pu et al. (2010, figs. 1 and 2). Here, we briefly describe the procedure for calibration of the atmospheric sky level. At the beginning, we selected the spectra of a galaxy where a sky spectrum with a uniform slit illumination was available and almost ideal photometric conditions were achieved, yielding the largest galaxy counts per pixel. To correct for the inhomogeneous slit illumination, we produced a 4th to 6th order polynomial model of the sky spectra for each column in the spatial direction and subtracted it from the selected galaxy frames, obtaining a reference frame $G_{\rm r}$. We computed the fractional residuals between the scaled and the reference slit profiles

$$R(r) = \left|1 - \frac{f_i^G \times \langle G_r \rangle}{\langle (G_i - f_i^{\rm S} \times {\rm SKY}_i) \rangle}\right| \tag{1}$$

and minimized it (see below). Here $f_i^{\rm S}$ is the scaling factor of the noise-free (i.e. the polynomial model) sky frame taken after the galaxy frame G_i, when available, or the average of the most uniform sky frames when not. The symbol $\langle\rangle$ indicates the average in the wavelength direction and $R(r)$ is a function of the position r along the slit. Moreover, f_r^G is a scaling factor that takes into account the different atmospheric transmissions. We determined f_i^G and $f_i^{\rm S}$ iteratively so as to minimize R, which in an ideal situation should be zero at every radii. Finally, we computed the resulting total galaxy frame $G_{\rm tot}$ as

$$G_{\rm tot} = G_r + \Sigma_i (G_i - f_i^{\rm S} \times {\rm SKY}_i)/f_i^G. \tag{2}$$

In practice, due to the non-uniformity of the slit illumination function, the function $R(r)$ is not always zero, but through the summing process in Equation (2) the differences should average out. We can test the quality of the calibration by comparing the profile $\langle G_{\rm tot} \rangle$ with available broadband photometry.

Figure 1 shows the comparison between the summed shifted slit profiles and the broadband photometry of the galaxy. The solid and open dots indicate the count number profiles measured from the summed spectrum of major and minor axes respectively. The solid and dashed lines present the V band photometry data taken from Kormendy et al. (2009). The plot confirms that the summed spectrum agrees well with the broadband photometry out to a large radius.

In addition, we also need to correct the anamorphic distortion of the LRS, remove the sky emission line spectrum and remove the continuum spectra. The procedures are described in detail in Pu et al. (2010).

3 KINEMATIC AND LICK/IDS INDEX PROFILES

3.1 Kinematics Profiles

We extracted the line-of-sight velocity distributions (LOSVDs) and kinematic parameters from the continuum-removed spectra that were rebinned radially to obtain almost constant signal-to-noise ratio, using the Fourier Correlation Quotient (FCQ) method (Bender 1990) with the implementation described in Saglia et al. (2010) that allows for the presence of emission lines. The stellar spectra library of Vazdekis (1999) is used as the templates aiming to minimize the mismatching. This library contains about a thousand synthetic single-stellar-population spectra covering the wavelength range from 4800 to 5470 Å with a resolution of 1.8 Å. We used the library with ages of 1.00 to 17.78 Gyr and metallicities from –1.68 to 0.2. We first set all of the library spectra to the resolution of our galaxy spectra and found the best fitting template for each radial bin according to the lowest RMS value of the residual (reaching typically 1% of the initial flux). If emission lines are detected, Gaussians are fitted to the residuals above the best-fit template and subtracted from the galaxy spectrum to derive cleaned spectra. The kinematic fit is then redone using these cleaned spectra. We did not detect emission in the spectra of NGC 4636.

Figure 2 presents the kinematics along the major and minor axes in NGC 4636. In this figure, we show the rotational velocity, the velocity dispersion and the Gauss-Hermite parameters H_3 and H_4.

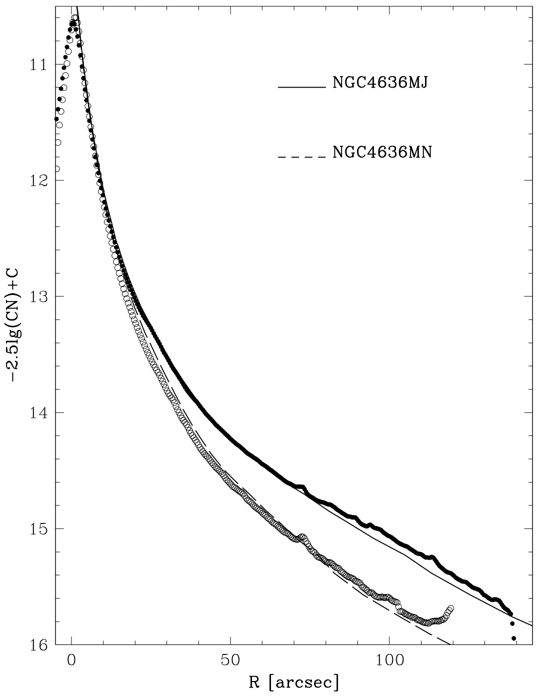

Fig. 1 Comparison between the broadband surface brightness profiles (lines) and the ones derived from our summed spectra (dots) for NGC 4636. The solid and open dots indicate the profiles measured from the summed spectrum along the major and minor axes respectively. The solid and dashed lines present the V band photometry data taken from Kormendy et al. (2009).

The filled and open symbols show the kinematic profiles on the south-east (SE) side along the major axis and the north-east (NE) side along the minor axis, respectively. The reference data taken from Bender et al. (1994) are also denoted by squares in the plot. As can be seen from the figures, agreement is generally good. Here, $a_{\mathrm{e}} = R_{\mathrm{e}} \cdot \epsilon^{-1/2}$ and $b_{\mathrm{e}} = R_{\mathrm{e}} \cdot \epsilon^{1/2}$ are labeled, where R_{e} is the effective radius and ϵ is the apparent axial ratio. The kinematic data extend to $140''$ along the major axis and 105 along the minor axis from the galaxy center. There are further extensions compared to the previous work of Bender et al. (1994); Davies et al. (1993); Rampazzo et al. (2005). The kinematic profiles present no rotation along either the major or minor axes. The velocity dispersion shows flat gradients inside $100''$ and becomes steep along the major axis. The measured stellar kinematics with an error table is presented in Table A.1 in Appendix.

3.2 Lick/IDS Index Profiles

In this section, we describe the measurement of six Lick/IDS indices (Hβ, Mgb, Fe$_{5015}$, Fe$_{5270}$, Fe$_{5335}$, Fe$_{5406}$), which were defined by Trager et al. (1998). The line strength indices have been measured from the cleaned spectra along the major and minor axes. Before measuring the indices, our spectra were degraded to the resolution of the Lick/IDS systems. We then corrected the indices for the velocity dispersion using template stars and the value for σ derived in the previous section. Finally, the observational data need to be corrected to the Lick/IDS system. To do this we observed five stars from the Lick/IDS library using the same instrumental configuration used for the science objects and derived the offsets between our data and the Lick/IDS system. The comparison of our

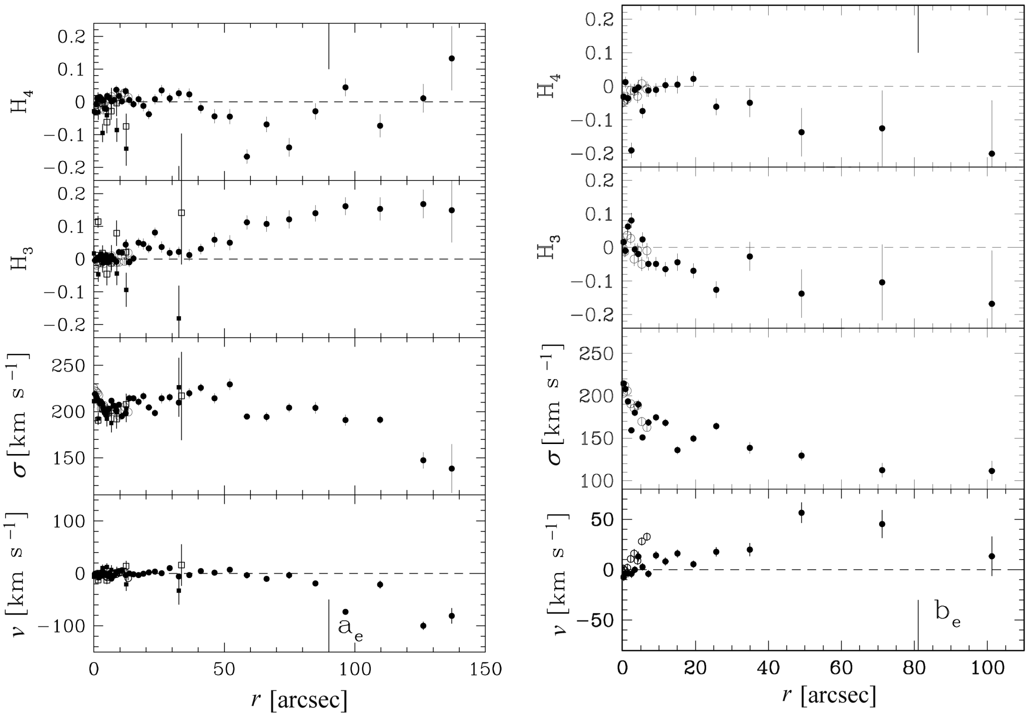

Fig. 2 Stellar kinematic profiles along the major and minor axes of NGC 4636. From bottom to top in each panel we show: (1) Rotation velocity, (2) Velocity dispersion, (3) and (4) Gauss-Hermite parameters H_3 and H_4 respectively. The profiles are folded with respect to the nucleus of the galaxies, and filled and open symbols stand for different sides of the galaxy. The squares show the data published in Bender et al. (1994).

data with the Lick standard systems can be found in Pu et al. (2010, fig. 4). The data are in good agreement with the Lick/IDS systems, as found in Saglia et al. (2010) using a larger set of Lick standards observed with LRS and HET at a better resolution. So far, the deviation between our measurements and the Lick system can be ignored, but we take into account the RMS of the calibration lines in the final error budget, by adding it in quadrature to the statistical error of each index.

Figure 3 shows the six line strength index profiles along the major and minor axes of the galaxy. The names and positions are labeled in the figure. The dots present the measured Lick/IDS values and the solid lines show the SSP model predictions; they will be discussed in the following sections. The full table of six Lick/IDS indices is presented in Table A.2 in the Appendix. The galaxy presents positive gradients of the Hβ index along both the major axis and minor axis, very similar to profiles in other galaxies discovered in previous work (Davies et al. 1993; Sánchez-Blázquez et al. 2007; Pu et al. 2010). We also measured the indices Mg_1 and Mg_2, but we do not use them in this work since these two indices are very sensitive to the anamorphic distortion.

4 STELLAR POPULATIONS

In this section, we derive the age, total metallicity and element abundance gradients along the major and minor axes by comparing the measured line indices with simple stellar population models (TMB03). The details of this model can be seen from Thomas et al. (2003, 2005). Here, we give a

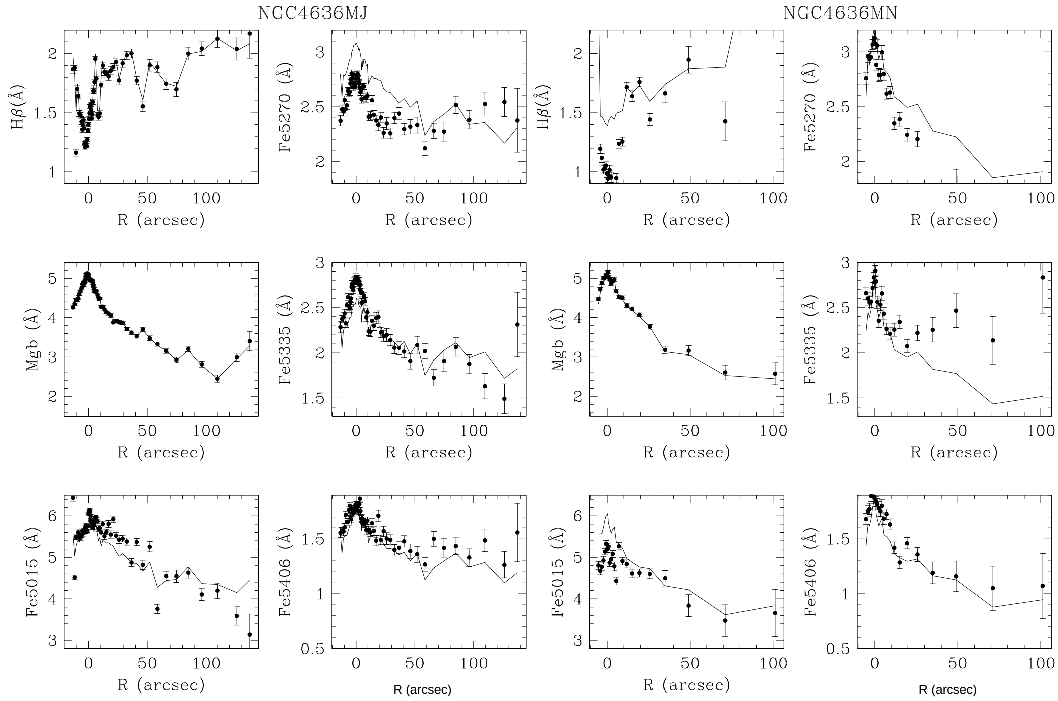

Fig. 3 Line-strength indices along the major and minor axes. The names of the indices are labeled and the galaxies' names are also noted. The solid lines show the model's (TMB03) predicted line strength profiles along the axes.

brief description of this model: The TMB03 models cover ages between 1 and 15 Gyr, and metallicities between 1/200 and 3.5 solar. Furthermore, the models take into account the effects on the Lick indices by the variation of α abundance and, hence, give Lick indices of simple stellar populations not only as a function of age and metallicity, but also as a function of the α/Fe ratio.

In this work, we do not adopt the traditional and effective method of studying stellar population properties which uses diagrams of different pairs of Lick indices (Thomas et al. 2005). The method selects the Hβ versus [MgFe]$'$ pair diagram to break the age-metallicity degeneracy, where $[\mathrm{MgFe}]' = \sqrt{\mathrm{Mg}b[0.72\mathrm{Fe}_{5270} + 0.28\mathrm{Fe}_{5335}]}$, because H$\beta$ is sensitive to warm turnoff stars and the [MgFe]$'$ index is considered as the best detector of metallicity since it does not depend on abundance ratio variations. Following Saglia et al. (2010) and Pu et al. (2010), we use the simple χ^2 minimization method. Here, the χ^2 method fits all of the Hβ, Mgb, Fe$_{5270}$, Fe$_{5335}$ and other available indices at the same time; the best resolution is bound to break the age-metallicity degeneracy. The tests for Coma galaxies done by Thomas et al. (2011) show that the results which were derived using the new method were better than the results obtained using the traditional method. The χ^2 is given by

$$\chi^2 = \sum_{\mathrm{index}[i]} \frac{(\mathrm{index}_{i[\mathrm{ob}]} - \mathrm{index}_{i[\mathrm{mod}]})^2}{(\sigma_{i[\mathrm{ob}]})^2}\,, \tag{3}$$

where index$_{i[\mathrm{ob}]}$ and index$_{i[\mathrm{mod}]}$ represent the ith observational indices and model indices respectively, and $\sigma_{i[\mathrm{ob}]}$ is the observational uncertainty of the ith indices. We can derive the best fitting age, metallicity and α/Fe by finding the minimum χ^2 of all selected line indices to the SSP models. The

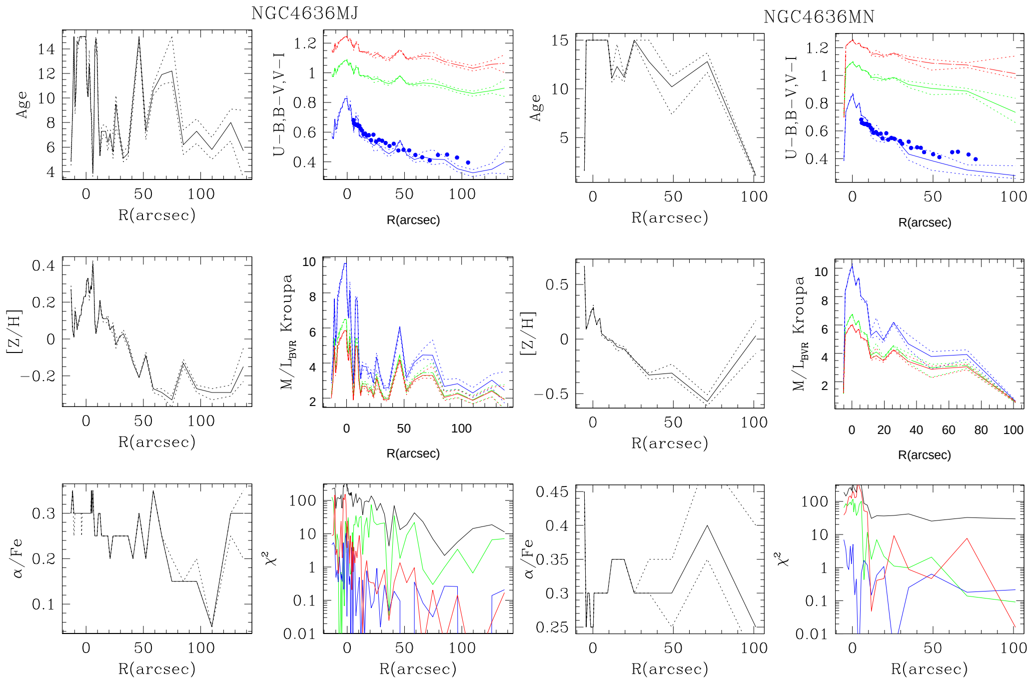

Fig. 4 Best fitting SSP equivalent age, metallicity and element abundance ratio are shown in the left of each plot. The right top of each plot shows the Johnson broadband $U-B$, $B-V$, and $V-I$ color profiles; the blue and green solid lines stand for $U-B$ and $B-V$ colors respectively; the red solid lines indicate the $V-I$ color. The measured $U-B$ color values taken from Peletier et al. (1990) are dotted with blue solid symbols. The M/L$_{BVI}$ are shown in the middle of the right columns, and the blue, green and red solid lines indicate the M/L in the B, V and I band respectively (color online); the minimized χ^2 of the selected line strengths are presented in the bottom panel on the right; red, blue and green lines present the minimized χ^2 of Hβ, Mgb and Fe$_{5270}$, respectively, while the black lines show the total minimized χ^2.

Hβ, Mgb, Fe$_{5015}$, Fe$_{5270}$, Fe$_{5335}$ and Fe$_{5406}$ are used as the indicators. Moreover, we interpolated the tabulated indices of TMB03 in steps of 0.1 Gyr for age, 0.02 for metallicity and 0.05 for α/Fe aiming to improve the precision of the stellar properties using the χ^2 minimization method.

Figure 4 presents the age predicted from the model, metallicity, element abundance, colors, mass-to-light ratios and resulting χ^2. From the top left panel to the bottom left panel, the age, total metallicity [Z/H] and α/Fe ratio are shown. The galaxy presents α overabundance from the galaxy center to the outer parts. The total metallicity profile shows a steep negative gradient with $\Delta[Z/H]/\Delta\log(r) = -0.333 \pm 0.022$ inside R_e and become flat outwards. The average age, metallicity and α/Fe inside 1/16 R_e are 9.96 ± 1.83 Gyr, 0.302 ± 0.08 and 0.325 ± 0.025 respectively. They are comparable to the results of age = 9.918 ±0.458 derived by Sánchez-Blázquez et al. (2006) using the Hβ versus [Mgb] pair diagram and the age $= 8.18 \pm 0.063$ in Proctor & Sansom (2002). The model predicted line strength profiles are shown in Figure 3 with solid lines. As can be seen from Figure 3, in general, theoretical line strength indices match well with the measured parameters in the inner regions of the galaxies except Fe$_{5270}$ due to these indices being contaminated by some unknown sky lines and we set its weight to zero. In addition, we also calculate the Johnson broadband $U-B$, $U-V$, $B-V$, $V-R$, $V-I$, $V-K$, $J-K$, $J-H$, and $H-K$ color and M/L ratio in B, V, R, I, J, H and K band profiles using the Kroupa initial mass function (Kroupa 1995) with the help of the SSP models (Maraston 1998). For a clear presentation in the figures, we only show the $U-B$, $B-V$ and $V-I$ colors and the mass to light ratios in B, V, and I bands in this paper. In the top right panels in Figure 4, the blue and green solid lines stand for $U-B$ and $B-V$ colors respectively; the red lines indicate the $V-I$ color. The measured $U-B$ color values (taken from Peletier et al. 1990) are also over plotted with solid blue dots. As can be seen from the plot, the predicted color profiles from the model agree well with the measured colors. Indeed, the colors present steep negative gradients and sharp peaks; this feature is mainly shaped by the metallicity profile. The middle right panel of Figure 4 shows the theoretical M/L ratio in B, V, and I bands; the blue, green and red lines display the M/L ratios in B, V and I colors respectively. The minimized χ^2 values of selected line strengths are presented in the bottom panel on the right. Red, blue and green lines present the minimized χ^2 of Hβ, Mgb and Fe_{5270} respectively, while the black lines show the total minimized χ^2. The large values of χ^2 along the major axis are mainly driven by the Fe_{5270}.

5 SUMMARY AND DISCUSSION

In this work, we measured the accurate kinematic profiles extending out to 1.5 R_e along the major and minor axes for the giant elliptical galaxy NGC 4636. Indeed, six Lick line indices (Hβ, Mgb, Fe_{5015}, Fe_{5270}, Fe_{5335}, Fe_{5406}) defined by Burstein et al. (1984); Worthey et al. (1994); Trager et al. (1998) of NGC 4636 are also derived. By comparing the measured Lick/IDS with the SSP model predictions, we derived the stellar population parameters, the M/L ratios and the broadband colors of our galaxies. We found the galaxy NGC 4636 has high metallicities in the galaxy center and presents steep negative metallicity gradients. The galaxy is α overabundant and does not present significant gradients of α abundances along the axes. The galaxy has sharp red peaks at the center which are mainly shaped by the metallicity (Maraston 1998). The colors predicted by the model agree well with the measured color profiles.

According to the simple element enrichment scenario, the α elements are mainly delivered by Type II supernovae explosions of massive progenitor stars and a substantial fraction of Fe peak elements come from the delayed exploding Type Ia supernovae (Nomoto et al. 1984; Thielemann et al. 1996). Thus the α/Fe can be used as an indicator to constrain the formation timescale of stars. Hence the flat profile of the α/Fe ratio in our galaxy likely suggests that there is no radial variation in star formation time scales. The radial metallicity and line strength gradients give one of the most stringent constraints on the galaxy formation (Sánchez-Blázquez et al. 2006; Tortora et al. 2011). The galaxies that form monolithically have steeper gradients and the galaxies that undergo major mergers have shallower gradients. The mean metallicity gradients for non-merger and merger galaxies derived by theoretical simulation in Kobayashi (2004) are Δ[Z/H]/$\Delta\log(r) \sim -0.30 \pm 0.2$ and -0.22 ± 0.2, respectively. The author found that the galaxies with gradients steeper than –0.35 are all not significant merger galaxies. The gradient inside R_e of NGC 4636 is $\Delta[Z/H]/\Delta\log(r) = -0.333 \pm 0.022$, while the gradient of NGC 4636 becomes flat outside of R_e. Accordingly, this is a weak indication that the center and the outer regions of NGC 4636 are formed through different formation processes. Indeed, it is worthwhile to observe the Lick/IDS in further out regions with a newly developed observing technique as was done by Weijmans et al. (2009). This research will give us new insight into the formation of the elliptical galaxies.

In the forthcoming works, we plan to further investigate the dynamical structure and orbit distribution of NGC 4636, in order to find further constraints on the formation process of the galaxy.

Appendix A: FULL TABLES OF MEASURED VALUES FOR GALAXY NGC 4636

Table A.1 Full table of measured stellar kinematics as a function of distance from the center for Galaxy NGC 4636 (positive: southeast, negative: northwest for the position angle of $150°$; and positive: northeast, negative: southwest for the position angle of $60°$).

PA (°)	R (″)	V (km s^{-1})	$\pm dV$ (km s^{-1})	σ (km s^{-1})	$\pm d\sigma$ (km s^{-1})	H_3	$\pm dH_3$	H_4	$\pm dH_4$	S/N
150	–13.17	–9.18	±3.36	199.4	±4.11	0.019	±0.015	0.014	±0.015	121.4
150	–11.77	3.97	±2.27	205.2	±2.87	–0.007	±0.010	0.028	±0.010	185.3
150	–10.60	2.26	±2.92	201.6	±3.64	0.011	±0.013	0.021	±0.013	141.2
150	–9.66	1.18	±2.55	195.3	±3.07	–0.010	±0.012	0.007	±0.012	156.8
150	–8.72	–1.21	±2.64	202.8	±3.13	–0.010	±0.012	0.003	±0.012	157.7
150	–7.78	–0.25	±2.66	205.1	±3.20	–0.004	±0.012	0.007	±0.012	157.9
150	–6.84	–0.67	±2.27	200.0	±2.79	0.010	±0.010	0.016	±0.010	180.2
150	–5.90	–2.00	±2.40	200.2	±2.91	0.000	±0.011	0.010	±0.011	170.7
150	–5.21	–7.68	±2.39	200.9	±2.72	0.007	±0.011	–0.014	±0.011	172.5
150	–4.74	–5.64	±2.75	201.4	±3.29	0.009	±0.012	0.006	±0.012	150.1
150	–4.27	–1.67	±2.48	204.2	±2.91	0.000	±0.011	–0.003	±0.011	168.5
150	–3.80	–0.92	±2.41	206.6	±2.67	–0.014	±0.011	–0.025	±0.011	175.5
150	–3.33	–0.78	±1.99	203.4	±2.25	–0.003	±0.009	–0.019	±0.009	208.9
150	–2.86	0.47	±2.28	203.3	±2.70	–0.011	±0.010	0.000	±0.010	182.7
150	–2.39	–1.07	±2.03	209.9	±2.43	–0.012	±0.009	0.006	±0.009	212.0
150	–1.92	–1.35	±1.93	217.7	±2.25	0.002	±0.008	–0.005	±0.008	231.5
150	–1.45	–0.03	±1.91	220.0	±2.17	–0.006	±0.008	–0.014	±0.008	236.2
150	–0.98	–2.39	±1.96	221.5	±2.31	–0.019	±0.008	–0.001	±0.008	231.3
150	–0.51	–2.28	±2.01	222.5	±2.41	–0.015	±0.008	0.007	±0.008	227.3
150	–0.04	–2.14	±2.08	225.6	±2.42	0.002	±0.008	–0.005	±0.008	222.5
150	0.44	–0.68	±1.90	219.1	±2.08	–0.004	±0.008	–0.031	±0.008	235.6
150	0.91	–3.11	±1.88	216.5	±2.18	–0.002	±0.008	–0.007	±0.008	235.7
150	1.38	–2.54	±1.98	213.3	±2.41	0.004	±0.008	0.012	±0.008	220.5
150	1.85	–2.33	±1.99	211.4	±2.40	–0.002	±0.009	0.008	±0.009	217.4
150	2.32	–5.90	±2.28	209.1	±2.79	0.007	±0.010	0.015	±0.010	188.0
150	2.79	–4.76	±2.23	210.2	±2.70	0.015	±0.010	0.010	±0.010	192.9
150	3.26	1.75	±2.59	208.6	±3.09	–0.003	±0.011	0.004	±0.011	164.9
150	3.73	1.93	±2.24	203.2	±2.68	–0.005	±0.010	0.005	±0.010	185.7
150	4.20	0.42	±2.21	198.8	±2.49	0.003	±0.010	–0.020	±0.010	183.9
150	4.67	–1.36	±2.54	196.4	±2.84	0.011	±0.012	–0.021	±0.012	158.4
150	5.14	–4.15	±2.72	201.7	±3.35	0.006	±0.012	0.018	±0.012	152.2
150	5.83	–0.15	±2.01	203.7	±2.45	–0.009	±0.009	0.013	±0.009	207.3
150	6.77	–9.65	±2.14	211.7	±2.54	0.010	±0.009	0.002	±0.009	202.3
150	7.71	–4.19	±2.37	206.3	±2.85	–0.001	±0.010	0.006	±0.010	178.1
150	8.65	1.46	±2.73	201.5	±3.52	–0.008	±0.012	0.037	±0.012	151.3
150	9.59	4.50	±2.46	207.4	±3.04	0.021	±0.011	0.018	±0.011	172.5
150	10.76	6.03	±2.50	195.1	±2.97	0.020	±0.012	0.002	±0.012	159.6
150	12.17	–3.08	±2.84	198.2	±3.63	0.044	±0.013	0.033	±0.013	142.9
150	13.58	0.00	±3.22	214.5	±3.87	–0.010	±0.014	0.006	±0.014	136.3
150	15.22	–1.65	±2.95	214.3	±3.42	0.002	±0.012	–0.007	±0.012	149.0
150	17.10	–3.33	±3.58	210.7	±4.32	0.050	±0.015	0.008	±0.015	120.6
150	18.98	–0.47	±3.98	216.8	±4.56	0.046	±0.017	–0.012	±0.017	111.6
150	21.09	2.07	±3.21	204.6	±3.44	0.033	±0.014	–0.038	±0.014	130.4
150	23.44	3.28	±3.34	198.5	±4.03	0.081	±0.015	0.008	±0.015	121.7
150	26.02	0.60	±4.12	214.4	±5.30	0.037	±0.017	0.035	±0.017	106.5
150	29.07	9.97	±3.61	215.5	±4.38	0.019	±0.015	0.011	±0.015	122.3
150	32.59	–5.76	±3.63	209.7	±4.57	0.022	±0.016	0.026	±0.016	118.4
150	36.58	–3.04	±4.25	219.8	±5.31	0.012	±0.018	0.023	±0.018	105.9
150	41.04	4.61	±4.10	225.8	±4.61	0.031	±0.016	–0.019	±0.016	112.9

Table A.1 — *Continued*

PA (°)	R ($''$)	V (km s^{-1})	$\pm$dV (km s^{-1})	σ (km s^{-1})	$\pm$dσ (km s^{-1})	H_3	$\pm$dH_3	H_4	$\pm$dH_4	S/N
150	46.20	1.35	±4.96	214.4	±5.22	0.059	±0.021	–0.044	±0.021	88.5
150	52.07	7.14	±5.81	229.5	±6.10	0.050	±0.023	–0.045	±0.023	80.9
150	58.63	–3.40	±4.45	194.6	±3.06	0.112	±0.021	–0.167	±0.021	89.6
150	66.15	–10.48	±4.84	194.2	±4.73	0.107	±0.023	–0.069	±0.023	82.2
150	74.81	–3.40	±6.26	204.3	±4.83	0.121	±0.028	–0.139	±0.028	66.9
150	84.90	–18.95	±5.63	204.1	±6.18	0.14	±0.025	–0.029	±0.025	74.3
150	96.40	–73.35	±4.50	190.8	±5.91	0.161	±0.027	0.044	±0.027	68.6
150	109.70	–21.30	±7.34	191.2	±4.34	0.153	±0.035	–0.073	±0.035	53.4
150	126.20	–99.93	±7.01	147.3	±8.52	0.168	±0.043	0.011	±0.043	43.0
150	137.18	–80.99	±14.87	138.3	±26.35	0.149	±0.098	0.133	±0.098	39.1
60	–5.29	28.13	±3.76	169.7	±4.53	–0.050	±0.020	0.008	±0.020	102.9
60	–4.13	9.01	±4.19	188.8	±4.57	–0.008	±0.020	–0.030	±0.020	102.8
60	–3.19	15.98	±4.05	185.4	±4.62	–0.035	±0.020	–0.014	±0.020	104.3
60	–2.25	10.58	±3.88	190.7	±4.45	0.027	±0.019	–0.012	±0.019	111.9
60	–1.31	1.93	±3.64	205.9	±3.89	0.036	±0.016	–0.038	±0.016	129.1
60	–0.61	–0.57	±3.66	212.1	±3.88	–0.013	±0.016	–0.041	±0.016	132.2
60	–0.14	1.11	±3.61	202.9	±3.77	–0.002	±0.016	–0.047	±0.016	128.3
60	0.33	–7.47	±3.83	214.5	±4.18	0.016	±0.016	–0.031	±0.016	127.5
60	0.80	–3.68	±3.89	208.0	±4.74	–0.010	±0.017	0.012	±0.017	121.8
60	1.49	–3.72	±4.08	193.4	±4.39	0.062	±0.019	–0.036	±0.019	108.0
60	2.43	–4.08	±3.89	159.3	±2.40	0.080	±0.022	–0.191	±0.022	93.4
60	3.37	0.00	±3.58	180.2	±4.12	–0.006	±0.018	–0.011	±0.018	114.6
60	4.31	13.04	±4.68	189.7	±5.49	–0.020	±0.022	–0.003	±0.022	92.3
60	5.47	2.68	±3.41	150.9	±3.29	0.024	±0.021	–0.074	±0.021	100.8
60	7.10	–4.08	±3.49	168.6	±4.00	–0.049	±0.019	–0.012	±0.019	110.1
60	9.20	14.11	±3.74	174.5	±4.30	–0.049	±0.020	–0.011	±0.020	106.2
60	11.77	8.18	±3.86	168.2	±4.59	–0.065	±0.021	0.003	±0.021	99.3
60	15.03	16.04	±3.92	136.0	±4.68	–0.044	±0.026	0.005	±0.026	90.3
60	19.46	5.39	±3.56	149.7	±4.44	–0.070	±0.022	0.022	±0.022	98.4
60	25.71	17.65	±4.58	164.2	±4.58	–0.126	±0.025	–0.061	±0.025	81.7
60	34.90	19.90	±6.52	138.7	±6.76	–0.027	±0.043	–0.049	±0.043	50.6
60	49.04	56.54	±10.23	129.6	∓6.04	–0.138	±0.072	–0.137	±0.072	35.8
60	71.14	45.24	±13.98	112.3	±8.26	–0.104	±0.113	–0.125	±0.113	24.7
60	101.22	13.33	±19.39	111.5	±11.46	–0.168	±0.158	–0.201	±0.158	16.6

Table A.2 Full table of measured Lick/IDS indices as a function of distance from the center for Galaxy NGC 4636 (positive: east, negative: west) for the different position angles.

PA (°)	R ($''$)	Mgb (Å)	Fe$_{5015}$ (Å)	Fe$_{5270}$ (Å)	Fe$_{5335}$ (Å)	Fe$_{5406}$ (Å)	Hβ (Å)
150	–13.17	4.262±0.039	6.434±0.081	2.374 2.284±0.062	1.557±0.045	1.869±0.033	
150	–11.77	4.341±0.026	4.515±0.055	2.478±0.031	2.375±0.040	1.577±0.030	1.880±0.022
150	–10.60	4.454±0.034	5.493±0.070	2.458±0.041	2.396±0.053	1.570±0.040	1.162±0.029
150	–9.66	4.445±0.030	5.497±0.062	2.562±0.037	2.436±0.047	1.606±0.035	1.702±0.026
150	–8.72	4.494±0.030	5.601±0.062	2.480±0.037	2.328±0.047	1.718±0.035	1.643±0.025
150	–7.78	4.597±0.030	5.520±0.062	2.514±0.037	2.529±0.047	1.655±0.036	1.494±0.025
150	–6.84	4.671±0.026	5.466±0.054	2.645±0.032	2.618±0.041	1.657±0.031	1.480±0.022
150	–5.90	4.752±0.028	5.532±0.057	2.632±0.034	2.517±0.043	1.766±0.033	1.425±0.024
150	–5.21	4.854±0.028	5.625±0.056	2.636±0.033	2.494±0.043	1.803±0.032	1.357±0.023
150	–4.74	4.811±0.032	5.573±0.065	2.712±0.038	2.565±0.050	1.705±0.037	1.393±0.027
150	–4.27	4.819±0.028	5.599±0.058	2.752±0.034	2.603±0.044	1.681±0.033	1.435±0.024
150	–3.80	4.898±0.027	5.644±0.056	2.804±0.033	2.730±0.043	1.769±0.032	1.368±0.023
150	–3.33	4.916±0.023	5.618±0.047	2.762±0.028	2.767±0.036	1.766±0.027	1.239±0.019

Table A.2 — *Continued*

PA (°)	R ($''$)	Mgb (Å)	Fe_{5015} (Å)	Fe_{5270} (Å)	Fe_{5335} (Å)	Fe_{5406} (Å)	Hβ (Å)
150	–2.86	4.957±0.026	5.702±0.053	2.712±0.031	2.726±0.041	1.742±0.031	1.208±0.022
150	–2.39	5.027±0.023	5.766±0.046	2.678±0.027	2.694±0.035	1.736±0.027	1.245±0.019
150	–1.92	5.099±0.021	5.708±0.043	2.795±0.025	2.769±0.033	1.770±0.025	1.221±0.017
150	–1.45	5.111±0.020	5.623±0.042	2.709±0.025	2.800±0.032	1.764±0.024	1.220±0.017
150	–0.98	5.125±0.021	5.640±0.043	2.680±0.025	2.811±0.033	1.780±0.025	1.273±0.018
150	–0.51	5.098±0.021	5.755±0.044	2.706±0.026	2.818±0.034	1.813±0.026	1.351±0.018
150	–0.04	5.083±0.022	6.045±0.044	2.759±0.026	2.841±0.035	1.811±0.026	1.400±0.018
150	0.44	5.008±0.020	6.095±0.042	2.774±0.025	2.811±0.032	1.816±0.024	1.449±0.017
150	0.91	4.957±0.020	6.140±0.042	2.794±0.025	2.827±0.032	1.795±0.024	1.498±0.017
150	1.38	4.950±0.022	6.113±0.045	2.803±0.026	2.792±0.034	1.762±0.026	1.553±0.018
150	1.85	4.964±0.022	5.986±0.046	2.759±0.027	2.818±0.035	1.755±0.026	1.571±0.018
150	2.32	4.958±0.025	5.866±0.053	2.719±0.031	2.796±0.040	1.756±0.030	1.528±0.022
150	2.79	4.950±0.025	5.835±0.051	2.712±0.030	2.750±0.039	1.816±0.029	1.453±0.021
150	3.26	4.919±0.029	5.722±0.059	2.671±0.035	2.697±0.045	1.868±0.034	1.488±0.024
150	3.73	4.876±0.026	5.716±0.052	2.634±0.031	2.756±0.040	1.755±0.030	1.592±0.022
150	4.20	4.814±0.026	5.797±0.053	2.656±0.031	2.668±0.040	1.685±0.030	1.683±0.022
150	4.67	4.741±0.030	5.791±0.061	2.570±0.036	2.555±0.046	1.654±0.035	1.685±0.025
150	5.14	4.669±0.031	5.849±0.065	2.674±0.038	2.668±0.049	1.688±0.037	1.759±0.026
150	5.83	4.650±0.023	5.973±0.047	2.688±0.028	2.567±0.036	1.661±0.027	1.957±0.019
150	6.77	4.682±0.024	5.972±0.048	2.686±0.029	2.636±0.037	1.633±0.028	1.789±0.020
150	7.71	4.580±0.027	5.867±0.056	2.585±0.033	2.572±0.042	1.644±0.032	1.479±0.023
150	8.65	4.478±0.032	5.693±0.064	2.580±0.038	2.394±0.049	1.582±0.037	1.464±0.027
150	9.59	4.490±0.028	5.702±0.057	2.600±0.034	2.451±0.044	1.666±0.033	1.494±0.023
150	10.76	4.279±0.030	5.600±0.061	2.409±0.036	2.239±0.047	1.580±0.035	1.736±0.025
150	12.17	4.280±0.033	5.802±0.069	2.418±0.041	2.235±0.052	1.561±0.039	1.900±0.028
150	13.58	4.208±0.036	5.506±0.072	2.560±0.043	2.355±0.056	1.643±0.042	1.844±0.029
150	15.22	4.137±0.033	5.612±0.066	2.427±0.039	2.300±0.051	1.573±0.038	1.829±0.027
150	17.10	4.105±0.040	5.803±0.083	2.376±0.049	2.386±0.063	1.485±0.047	1.808±0.033
150	18.98	4.056±0.044	5.549±0.088	2.335±0.052	2.398±0.068	1.712±0.051	1.857±0.036
150	21.09	3.880±0.037	5.920±0.075	2.403±0.044	2.227±0.057	1.491 ±0.043	1.887±0.031
150	23.44	3.915±0.039	5.522±0.080	2.263±0.048	2.190±0.062	1.570±0.046	1.930±0.033
150	26.02	3.884±0.046	5.426±0.093	2.349±0.055	2.199±0.072	1.503±0.054	1.774±0.038
150	29.07	3.870±0.040	5.451±0.081	2.258±0.049	2.142±0.062	1.492±0.047	1.918±0.033
150	32.59	3.710±0.041	5.381±0.085	2.398 ±0.049	2.058±0.064	1.401±0.048	1.987±0.034
150	36.58	3.620±0.046	4.876±0.096	2.439±0.056	2.056±0.073	1.420±0.055	2.002±0.038
150	41.04	3.529±0.044	5.369±0.088	2.297±0.052	2.017±0.070	1.478±0.052	1.772±0.036
150	46.20	3.705±0.055	4.820±0.112	2.319±0.066	1.908±0.087	1.389±0.065	1.554±0.045
150	52.07	3.483±0.061	5.256±0.124	2.334±0.073	2.086±0.098	1.360±0.073	1.902±0.050
150	58.63	3.330±0.054	3.758±0.112	2.123±0.065	2.021±0.082	1.268±0.062	1.885±0.045
150	66.15	3.156±0.059	4.549±0.119	2.281±0.071	1.724±0.090	1.501±0.067	1.746±0.049
150	74.81	2.927±0.073	4.546±0.150	2.274±0.087	1.910±0.112	1.419±0.084	1.698±0.060
150	84.90	3.210±0.066	4.632±0.133	2.518±0.079	2.067±0.102	1.435±0.075	2.001±0.054
150	96.40	2.813±0.071	4.104±0.143	2.383±0.085	1.877±0.107	1.331±0.080	2.043±0.058
150	109.70	2.452±0.092	4.197±0.183	2.526±0.109	1.631±0.140	1.487±0.103	2.127±0.075
150	126.20	2.995±0.110	3.588±0.221	2.544±0.132	1.493±0.163	1.265±0.120	2.040±0.093
150	137.18	3.403±0.243	3.139±0.494	2.376±0.290	2.315±0.357	1.559±0.266	2.171±0.209
60	–5.290	4.474±0.045	4.803±0.094	2.761±0.055	2.661±0.068	1.681±0.051	2.792±0.039
60	–4.13	4.720±0.046	4.676±0.096	2.962±0.056	2.600±0.072	1.754±0.053	1.195±0.040
60	–3.19	4.884±0.045	4.773±0.094	2.936±0.055	2.556±0.070	1.774±0.052	1.117±0.039
60	–2.25	5.009±0.043	4.928±0.088	2.952±0.052	2.566±0.066	1.892±0.049	1.019±0.037
60	–1.31	5.019±0.037	5.138±0.079	3.068±0.045	2.719±0.058	1.941±0.043	1.028±0.032
60	–0.61	5.070±0.036	5.329±0.077	3.101±0.044	2.835±0.057	1.886±0.043	1.053±0.031
60	–0.14	5.090±0.037	5.196±0.079	3.128±0.045	2.784±0.058	1.870±0.044	0.984±0.032
60	0.33	5.160±0.038	5.202±0.079	3.075±0.046	2.908±0.060	1.953±0.045	0.941±0.032
60	0.80	5.028±0.039	5.259±0.082	2.882±0.048	2.791±0.062	1.842±0.046	0.969±0.034
60	1.49	4.986±0.044	4.869±0.091	3.058±0.053	2.561±0.068	1.817±0.051	1.017±0.038

Table A.2 — *Continued*

PA (°)	R ($''$)	Mgb (Å)	Fe$_{5015}$ (Å)	Fe$_{5270}$ (Å)	Fe$_{5335}$ (Å)	Fe$_{5406}$ (Å)	Hβ (Å)
60	2.43	4.869±0.049	4.955±0.102	2.790±0.060	2.355±0.074	1.784±0.056	0.953±0.044
60	3.37	4.922±0.041	5.081±0.086	2.791±0.050	2.534±0.063	1.752±0.047	0.717±0.036
60	4.31	4.966±0.051	4.781±0.106	2.997±0.063	2.658±0.080	1.803±0.059	0.719±0.044
60	5.47	4.675±0.046	4.430±0.094	2.798±0.055	2.433±0.068	1.684±0.051	0.946±0.040
60	7.10	4.527±0.042	5.267±0.087	2.620±0.051	2.266±0.064	1.726±0.048	1.237±0.037
60	9.20	4.507±0.044	4.910±0.091	2.631±0.054	2.211±0.067	1.632±0.050	1.255±0.038
60	11.77	4.309±0.047	4.841±0.097	2.349±0.057	2.257±0.072	1.420±0.053	1.716±0.041
60	15.03	4.223±0.051	4.611±0.104	2.387±0.062	2.343±0.075	1.286±0.056	1.640±0.045
60	19.46	4.075±0.047	4.622±0.097	2.245±0.057	2.076±0.070	1.461±0.052	1.759±0.041
60	25.71	3.768±0.057	4.601±0.118	2.205±0.070	2.221±0.086	1.358±0.064	1.443±0.050
60	34.90	3.186±0.092	4.497±0.188	1.677±0.112	2.255±0.135	1.191±0.100	1.664±0.080
60	49.04	3.164±0.130	3.836±0.265	1.775±0.157	2.467±0.186	1.159±0.140	1.949±0.113
60	71.14	2.607±0.188	3.477±0.381	0.940±0.223	2.139±0.266	1.051±0.201	1.427±0.165
60	101.22	2.575±0.279	3.659±0.568	0.478±0.336	2.835 ±0.395	1.071±0.296	3.797±0.239

Acknowledgements We especially thank the McDonald Observatory for performing the observations with the Hobby-Eberly Telescope (HET) in service mode. The HET is a joint project of the University of Texas at Austin, the Pennsylvania State University, Stanford University, Ludwig-Maximilians-Universität München and Georg-August-Universität Göttingen. The HET is named in honor of its principal benefactors, William P. Hobby and Robert E. Eberly. The Marcario Low Resolution Spectrograph is named for Mike Marcario of High Lonesome Optics who fabricated several optics for the instrument but died before its completion. The LRS is a joint project of the Hobby-Eberly Telescope partnership and the Instituto de Astronomía de la Universidad Nacional Autónoma de México. This work was in part supported by the National Natural Science Foundation of China (Grant No. 10821061) and the National Basic Research Program of China (Grant Nos. 11033008 and 2007CB815406). We also gratefully acknowledge the Chinese Academy of Sciences and Max-Planck-Institut für extraterrestrische Physik that partially supported this work. Z. Han thanks the support of the Chinese Academy of Sciences (Grant No. KJCX2-YW-T24). We thank Prof. Bender who gave us the HET time to perform the observations. We are grateful to Dr. R. P. Saglia and J. Thomas for reading the manuscript and providing useful suggestions. We really appreciate the referee for the useful comments that helped us to improve the presentation of the results.

References

Annibali, F., Bressan, A., Rampazzo, R., & Zeilinger, W. W. 2006, A&A, 445, 79
Barnes, J. E. 1992, ApJ, 393, 484
Bell, E. F., Wolf, C., Meisenheimer, K., et al. 2004, ApJ, 608, 752
Bender, R. 1990, A&A, 229, 441
Bender, R., Burstein, D., & Faber, S. M. 1992, ApJ, 399, 462
Bender, R., Burstein, D., & Faber, S. M. 1993, ApJ, 411, 153
Bender, R., Saglia, R. P., & Gerhard, O. E. 1994, MNRAS, 269, 785
Bender, R., Saglia, R. P., Ziegler, B., et al. 1998, ApJ, 493, 529
Bender, R., & Surma, P. 1992, A&A, 258, 250
Bender, R., Surma, P., Doebereiner, S., Moellenhoff, C., & Madejsky, R. 1989, A&A, 217, 35
Bernardi, M., Nichol, R. C., Sheth, R. K., Miller, C. J., & Brinkmann, J. 2006, AJ, 131, 1288
Burstein, D., Faber, S. M., Gaskell, C. M., & Krumm, N. 1984, ApJ, 287, 586
Chakrabarty, D., & Raychaudhury, S. 2008, AJ, 135, 2350
Clemens, M. S., Bressan, A., Nikolic, B., et al. 2006, MNRAS, 370, 702
Collobert, M., Sarzi, M., Davies, R. L., Kuntschner, H., & Colless, M. 2006, MNRAS, 370, 1213

Davies, R. L., Sadler, E. M., & Peletier, R. F. 1993, MNRAS, 262, 650
De Lucia, G., Springel, V., White, S. D. M., Croton, D., & Kauffmann, G. 2006, MNRAS, 366, 499
Denicoló, G., Terlevich, R., Terlevich, E., Forbes, D. A., & Terlevich, A. 2005, MNRAS, 358, 813
Dirsch, B., Schuberth, Y., & Richtler, T. 2005, A&A, 433, 43
Djorgovski, S., & Davis, M. 1987, ApJ, 313, 59
Dressler, A., Lynden-Bell, D., Burstein, D., et al. 1987, ApJ, 313, 42
Faber, S. M., Willmer, C. N. A., Wolf, C., et al. 2007, ApJ, 665, 265
Fisher, D., Franx, M., & Illingworth, G. 1995, ApJ, 448, 119
Hill, G. J., MacQueen, P. J., Nicklas, H., et al. 1998, in American Astronomical Society Meeting Abstracts, Bulletin of the American Astronomical Society, vol. 30, 1262
Hopkins, P. F., Cox, T. J., Dutta, S. N., et al. 2009, ApJS, 181, 135
Kauffmann, G., White, S. D. M., & Guiderdoni, B. 1993, MNRAS, 264, 201
Kim, E., Kim, D., Fabbiano, G., et al. 2006, ApJ, 647, 276
Kobayashi, C. 2004, MNRAS, 347, 740
Kormendy, J., Fisher, D. B., Cornell, M. E., & Bender, R. 2009, ApJS, 182, 216
Kroupa, P. 1995, ApJ, 453, 350
Kuntschner, H. 2000, MNRAS, 315, 184
Larson, R. B. 1975, MNRAS, 173, 671
Larson, R. B. 1976, MNRAS, 176, 31
Lee, M. G., Park, H. S., Hwang, H. S., et al. 2010, ApJ, 709, 1083
Li, Z., Han, Z., & Zhang, F. 2007, A&A, 464, 853
Lisker, T., & Han, Z. 2008, ApJ, 680, 1042
Maraston, C. 1998, MNRAS, 300, 872
Matković, A., Guzmán, R., Sánchez-Blázquez, P., et al. 2009, ApJ, 691, 1862
Mehlert, D., Saglia, R. P., Bender, R., & Wegner, G. 1998, A&A, 332, 33
Nieto, J., & Bender, R. 1989, A&A, 215, 266
Nolthenius, R. 1993, ApJS, 85, 1
Nomoto, K., Thielemann, F., & Yokoi, K. 1984, ApJ, 286, 644
O'Sullivan, E., Vrtilek, J. M., & Kempner, J. C. 2005, ApJ, 624, L77
Park, H. S., Lee, M. G., Hwang, H. S., et al. 2010, ApJ, 709, 377
Peletier, R. F., Davies, R. L., Illingworth, G. D., Davis, L. E., & Cawson, M. 1990, AJ, 100, 1091
Posson-Brown, J., Raychaudhury, S., Forman, W., Donnelly, R. H., & Jones, C. 2009, ApJ, 695, 1094
Proctor, R. N., & Sansom, A. E. 2002, MNRAS, 333, 517
Pu, S. B., Saglia, R. P., Fabricius, M. H., et al. 2010, A&A, 516, A4
Rampazzo, R., Annibali, F., Bressan, A., et al. 2005, A&A, 433, 497
Rembold, S. B., Pastoriza, M. G., Ducati, J. R., Rubio, M., & Roth, M. 2002, A&A, 391, 531
Rogers, B., Ferreras, I., Pasquali, A., et al. 2010, MNRAS, 405, 329
Saglia, R. P., Bender, R., & Dressler, A. 1993, A&A, 279, 75
Saglia, R. P., Fabricius, M., Bender, R., et al. 2010, A&A, 509, A61
Sánchez-Blázquez, P., Forbes, D. A., Strader, J., Brodie, J., & Proctor, R. 2007, MNRAS, 377, 759
Sánchez-Blázquez, P., Gorgas, J., Cardiel, N., & González, J. J. 2006, A&A, 457, 809
Sánchez-Blázquez, P., Jablonka, P., Noll, S., et al. 2009, A&A, 499, 47
Schuberth, Y., Richtler, T., Dirsch, B., et al. 2006, A&A, 459, 391
Somerville, R. S., & Primack, J. R. 1999, MNRAS, 310, 1087
Tantalo, R., Chiosi, C., & Bressan, A. 1998, A&A, 333, 419
Tantalo, R., Chiosi, C., Bressan, A., & Fagotto, F. 1996, A&A, 311, 361
Thielemann, F., Nomoto, K., & Hashimoto, M. 1996, ApJ, 460, 408
Thomas, D. 1999, MNRAS, 306, 655

Thomas, D., Maraston, C., & Bender, R. 2003, MNRAS, 339, 897
Thomas, D., Maraston, C., Bender, R., & Mendes de Oliveira, C. 2005, ApJ, 621, 673
Thomas, J., Saglia, R. P., Bender, R., et al. 2011, arXiv:1103.3414
Tinsley, B. M. 1972, ApJ, 178, 319
Tinsley, B. M. 1980, Fund. Cosmic Phys., 5, 287
Tonry, J. L., Dressler, A., Blakeslee, J. P., et al. 2001, ApJ, 546, 681
Tortora, C., Romeo, A. D., Napolitano, N. R., et al. 2011, MNRAS, 411, 627
Trager, S. C., Faber, S. M., Worthey, G., & González, J. J. 2000, AJ, 119, 1645
Trager, S. C., Worthey, G., Faber, S. M., Burstein, D., & Gonzalez, J. J. 1998, ApJS, 116, 1
Vazdekis, A. 1999, ApJ, 513, 224
Weijmans, A., Cappellari, M., Bacon, R., et al. 2009, MNRAS, 398, 561
White, S. D. M. 1980, MNRAS, 191, 1P
White, S. D. M., & Frenk, C. S. 1991, ApJ, 379, 52
White, S. D. M., & Rees, M. J. 1978, MNRAS, 183, 341
Worthey, G., Faber, S. M., Gonzalez, J. J., & Burstein, D. 1994, ApJS, 94, 687
Ziegler, B. L., & Bender, R. 1997, MNRAS, 291, 527